IEICE TRANS. COMMUN., VOL.E99–B, NO.1 JANUARY 2016

PAPER Special Section on Recent Progress in Antennas, Propagation and Wireless Systems Related to Topics in ISAP2014

False Image Suppression in Two-Dimensional Shape Estimates of a Walking Human Using Multiple Ultra-Wideband Doppler Radar Interferometers

Hiroki YAMAZAKI[†a)], ***Student Member***, **Takuya SAKAMOTO**[††], **Hirofumi TAKI**[†††], ***Members***, ***and*** **Toru SATO**[†], ***Fellow***

SUMMARY Microwave systems have a number of promising applications in surveillance and monitoring systems. The main advantage of microwave systems is their ability to detect targets at distance under adverse conditions such as dim, smoky, and humid environments. Specifically, the wide bandwidth of ultra-wideband radar enables high range resolution. In a previous study, we proposed an accurate shape estimation algorithm for multiple targets using multiple ultra-wideband Doppler interferometers. However, this algorithm produces false image artifacts under conditions with severe interference. The present paper proposes a technique to suppress such false images by detecting inconsistent combinations of the radial velocity and time derivative of image positions. We study the performance of the proposed method through numerical simulations of a two-dimensional section of a moving human body, and demonstrate the remarkable performance of the proposed method in suppressing false image artifacts in many scenarios.

key words: *ultra-wideband radar, multiple interferometers, Doppler radar, walking human, shape estimation, false image rejection*

1. Introduction

In modern society, there is a wide range of applications for techniques that automatically monitor human movements, such as the prevention of terrorism and home healthcare. At present, many automatic monitoring systems use optical cameras [1], [2]. However, optical cameras cannot accurately identify the distance between the target and the camera, and cannot work in adverse conditions such as dim, smoky, and humid environments.

The high range resolution capability of ultra-wideband (UWB) radar represents a promising means of overcoming these difficulties. A number of UWB radar imaging algorithms have been proposed. For example, back-propagation imaging algorithms [3]–[5] are widely applied because of their simple processing. However, to reconstruct a detailed target shape, the back-propagation imaging algorithm requires large-scale array antennas or mechanical scanners, leading to bulky and costly systems. To solve this problem, inverse synthetic aperture radar (ISAR) imaging algorithms [6], [7] have been developed. Although ISAR imaging algorithms exploit target motion instead of scanning antennas, they are mainly designed for targets with simple motion such as rotation and translation, and are therefore unsuitable for the imaging of human bodies in motion.

We have already proposed a UWB imaging method using a small number of antennas [8]. This uses multiple interferometers [9] to estimate the scattering centers of targets in multiple directions [10]. By clustering the radial velocities, the algorithm determines which target these scattering centers belong to. Finally, the method estimates the whole target image by applying motion compensation to the classified scattering centers. Although our previous method can estimate accurate target shapes using only a small number of antennas, this method is limited by false image artifacts under conditions with severe echo interference from different targets. This drawback significantly reduces the method's reliability in certain applications.

To overcome this problem, we now propose a false image suppression method that exploits two means of estimating the target velocity. The proposed method rejects false estimated images by detecting inconsistent combinations of the radial velocity and time derivative of the image positions, and estimates a clear image of multiple targets as a result of improved accuracy [8]. In this paper, we first explain the conventional UWB Doppler radar imaging method, and confirm that false images are output when the scattering centers are misclassified. We then explain our proposed method, and verify its remarkable performance using numerical simulations.

2. System Model

Figure 1 illustrates our indoor surveillance system. We assume that a person walks in a straight line within a room, and set six interferometers on the ceiling at 2 m intervals. Each interferometer is composed of one transmitter and two receivers. The two receivers are 5.0 mm apart in the x direction, corresponding to approximately half a wavelength, and the transmitter is located halfway between the receivers. The system model assumed in this study uses antennas with a fan beam that has high and low directivities in the vertical

Manuscript received April 6, 2015.
Manuscript revised August 17, 2015.

[†]The authors are with the Department of Communications and Computer Engineering, Graduate School of Informatics, Kyoto University, Kyoto-shi 606-8501 Japan.
[††]The author is with Graduate School of Engineering, University of Hyogo, Himeji-shi, 671-2280 Japan.
[†††]The author is with the Department of Electronic Engineering, Graduate School of Engineering, Tohoku University, Sendai-shi, 980-8579 Japan.
a) E-mail: hyamazaki@sato-lab.0t0.jp

DOI: 10.1587/transcom.2015ISP0024

Copyright © 2016 The Institute of Electronics, Information and Communication Engineers

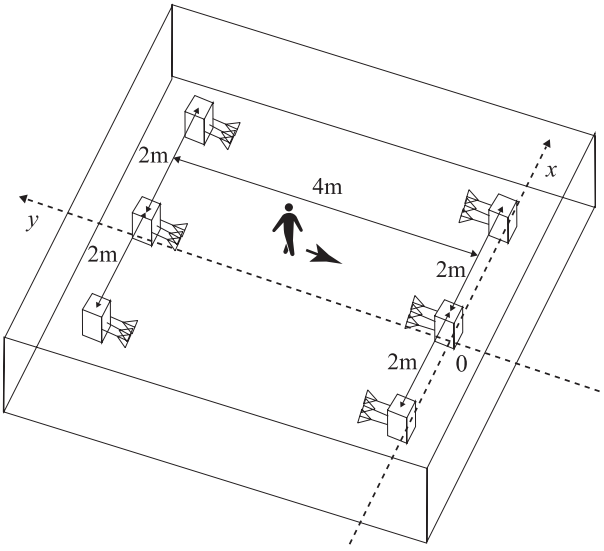

Fig. 1 Indoor surveillance system used in this study to model a person walking through a room.

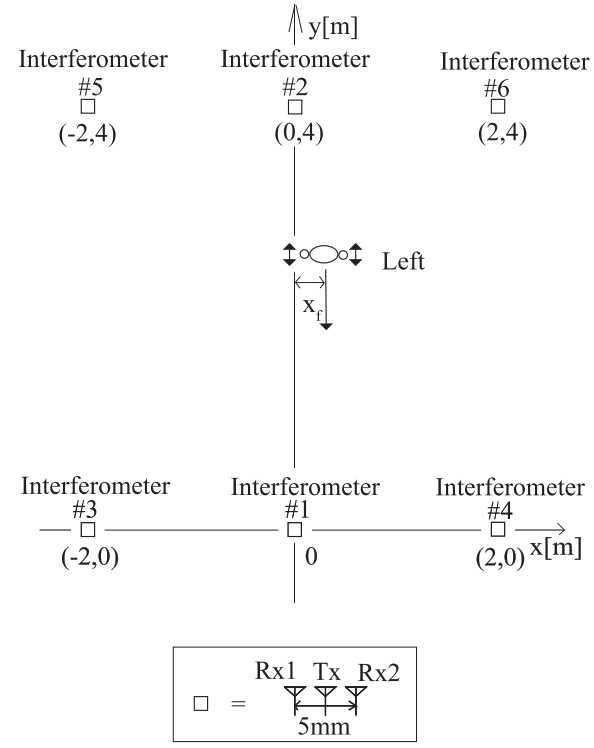

Fig. 2 Two-dimensional model approximated from Fig. 1 that is considered in this study.

and horizontal directions, respectively. Therefore, we assume that the beam covers only the torso and arms. Under this assumption, the 3-dimensional model in Fig. 1 can be approximated as the 2-dimensional model shown in Fig. 2. For simplicity, we consider this 2-dimensional problem. We assume that some method of signal separation is used to ensure that the transmitter pulses do not interfere with each other. The radar has a 26.4 GHz center frequency, 730 MHz -10 dB bandwidth, and 1.3 ms pulse interval.

We consider the cross-section of a walking person with time-varying velocities as in Fig. 3. For simplicity, the torso is modeled as an ellipse, and the arms are modeled as circles. The circular and elliptical target models in our 2-dimensional scenario correspond to circular and elliptical cylinders in an actual 3-dimensional scenario. Various human models are reviewed in [11] and [12]. The center of the torso $(X_a(t), Y_a(t))$, center of the left arm $(X_b(t), Y_b(t))$, and center of the right arm $(X_c(t), Y_c(t))$ move with time t according to

$$X_a(t) = x_f \tag{1}$$
$$Y_a(t) = -V_f t + y_f \tag{2}$$
$$X_b(t) = x_f - l_f \tag{3}$$
$$Y_b(t) = Y_a(t) - A_f \sin(2\pi t/T_f) \tag{4}$$
$$X_c(t) = x_f + l_f \tag{5}$$
$$Y_c(t) = Y_a(t) + A_f \sin(2\pi t/T_f), \tag{6}$$

where x_f is the offset of movement along the x-axis, y_f is the offset of movement along the y-axis, l_f is the distance between the center of the torso and the center of the arms, V_f is the velocity of the torso, A_f is the amplitude with which the arms swing, and T_f represents the period of the swinging motion. The rotation period of the torso corresponds to the period with which the arms are swinging. The rotation angle $\omega_f(t)$ is expressed as

$$\omega_f(t) = \theta_{f0} \sin(2\pi t/T_f), \tag{7}$$

where θ_{f0} is the maximum rotation angle. We set $x_f = 0.3$ m, $y_f = 2.8$ m, $l_f = 0.2$ m, $V_f = 1.32$ m/s, $A_f = 0.3$ m, and $T_f = 1.41$ s. In addition, we set θ_{f0} to 10°, which is representative of an actual walking human [13], [14]. Under these conditions, we perform a series of ray tracing numerical simulations. In our ray-tracing simulations, we consider only a single reflection without multipath echoes. We do not consider penetration or diffraction, either. The targets are modeled with perfect electric conductor.

In our simulations, we evaluate the signal quality using the signal-to-noise ratio (S/N) instead of signal-to-interference ratio (S/I). This is because signal and interference components cannot be separated, considering that all echoes are reflections from various parts of a human body. All the echoes are, therefore, necessary in estimating the target shape.

3. Conventional Methods

3.1 Position Estimation and Target Velocity Estimation Using Doppler Radar Interferometric Imager

A UWB Doppler radar imager [10] separates multiple scattering centers in the time-frequency domain, and then estimates their positions. If different scattering centers have different radial velocities, they can be separated using the difference in their Doppler frequencies. To determine the

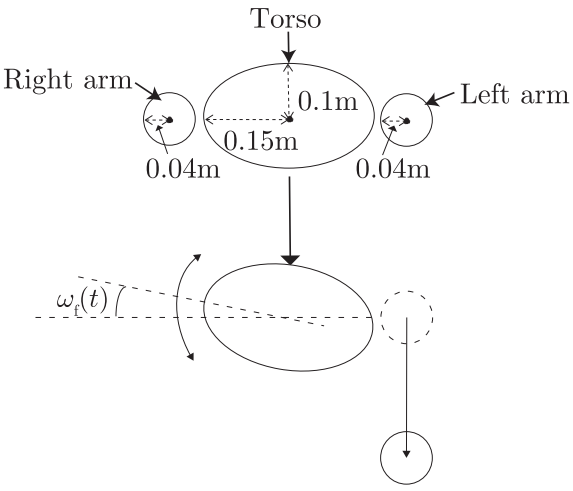

Fig. 3 Human body model used in our study.

Doppler frequencies, we apply a short-time Fourier transform (STFT) to the received signal. After separation, we then estimate the position of the scattering center for each echo. We estimate the distance to the target using range interpolation, and seek the range that maximizes the echo intensity. We also use interferometry to estimate the direction-of-arrival; details can be found in Appendix. From this distance and direction-of-arrival information, the position of the scattering center can be estimated. The correspondence between the estimated scattering centers and targets is unknown, and so the range of the estimated image is restricted. To overcome this problem, we estimate the target velocity from a combination of radial velocities.

Let $\boldsymbol{v}$ be the actual velocity vector of the target, and $\boldsymbol{i}_{i_1}^{m_1}$ and $\boldsymbol{i}_{i_2}^{m_2}$ be the unit radial vectors from the i_j-th interferometer to the m_j-th scattering center $\boldsymbol{x}_{i_j}^{m_j}$ for j = 1 and 2, respectively. The equations

$$\begin{cases} \boldsymbol{v}^{\mathrm{T}}\boldsymbol{i}_{j_1}^{m_1} = v_{j_1}^{m_1} \\ \boldsymbol{v}^{\mathrm{T}}\boldsymbol{i}_{j_2}^{m_2} = v_{j_2}^{m_2} \end{cases} \quad \text{and} \tag{8}$$

then hold [8], where $^{\mathrm{T}}$ is the transpose operator. Equation (8) estimates the correct $\boldsymbol{v}$, regardless of i_1,i_2,m_1, and m_2, if $\boldsymbol{x}_{i_1}^{m_1}$ and $\boldsymbol{x}_{i_2}^{m_2}$ belong to the same target. However, Eq. (8) estimates an incorrect $\boldsymbol{v}$ if $\boldsymbol{x}_{i_1}^{m_1}$ and $\boldsymbol{x}_{i_2}^{m_2}$ belong to different targets.

3.2 Scattering Center Classification Using a Clustering Algorithm in the Velocity Space

In this section, we classify the scattering centers based on the principle explained in the previous section. First, we apply Eq. (8) for all combinations of i_1, i_2, m_1, and m_2, and estimate the velocity candidates in the v_x-v_y space. We then extract dense candidate sets as clusters, because the candidates that have been estimated correctly will be dense. The density-based spatial clustering of applications with noise (DBSCAN) [15] is appropriate in this case, because it not

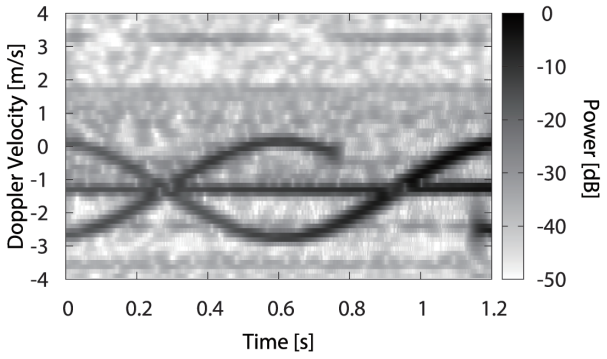

Fig. 4 Interferometer 1 spectrogram calculated using the STFT.

only separates the given data points into multiple clusters, but also rejects points that do not form any dense clusters. DBSCAN first selects a point $\boldsymbol{p}$, and then calculates $N(\boldsymbol{p})$, which is the set of points within a distance D of $\boldsymbol{p}$. The DBSCAN algorithm then determines the density-reachable point q that satisfies

1. $\boldsymbol{q} \in N(\boldsymbol{p})$
2. $|N(\boldsymbol{p})| \geq N_{\min}$,

where $N_{\min}$ is the threshold for the number of points. DBSCAN repeats these steps and extracts the density-reachable points as a cluster. We first apply DBSCAN in the $v_x - v_y$ space, and then apply it to the median value of the extracted clusters in the $v_x - v_y - t$ space to remove falsely extracted clusters. We define the proximity as an ellipsoid with major axis D_{a} and minor axis D_{b} in the $v_x - v_y - t$ space, and define the threshold for the number of points as $N'_{\min}$.

Next, we apply $\alpha - \beta$ filter tracking [16] to the median value $\boldsymbol{v}_n$ of the velocities extracted as cluster n by DBSCAN. The $\alpha - \beta$ filter is expressed as

$$\boldsymbol{v}_{sn}(t_k) = \boldsymbol{v}_{\mathrm{p}n}(t_{k-1}) + \alpha(\boldsymbol{v}_n(t_k) - \boldsymbol{v}_{\mathrm{p}n}(t_k)) \tag{9}$$

$$\boldsymbol{a}_{sn}(t_k) = \boldsymbol{a}_{\mathrm{p}n}(t_{k-1}) + \beta\frac{(\boldsymbol{v}_n(t_k) - \boldsymbol{v}_{\mathrm{p}n}(t_k))}{\Delta t} \tag{10}$$

$$\boldsymbol{v}_{\mathrm{p}n}(t_k) = \boldsymbol{v}_{sn}(t_{k-1}) + \Delta t\boldsymbol{a}_{sn}(t_{k-1}) \tag{11}$$

$$\boldsymbol{a}_{\mathrm{p}n}(t_k) = \boldsymbol{a}_{sn}(t_{k-1}), \tag{12}$$

where t_k is the discretization time given by Δt, $\boldsymbol{v}_{sn}(t_k) = (v_{\mathrm{sx}n}(t_k), v_{\mathrm{sy}n}(t_k))$ is the smoothed velocity, $\boldsymbol{v}_{\mathrm{p}n}(t_k) = (v_{\mathrm{px}n}(t_k), v_{\mathrm{py}n}(t_k))$ is the predicted velocity, $\boldsymbol{a}_{sn}(t_k) = (a_{\mathrm{sx}n}(t_k), a_{\mathrm{sy}n}(t_k))$ is the smoothed acceleration, and $\boldsymbol{a}_{\mathrm{p}n}(t_k) = (a_{\mathrm{px}n}(t_k), a_{\mathrm{py}n}(t_k))$ is the predicted acceleration. If the $\alpha - \beta$ filter tracks $\boldsymbol{v}_{\mathrm{n}}$ correctly, the classification results are correctly connected in the time domain. Finally, we apply motion compensation [9] to the classified scattering centers, and estimate the target image.

3.3 Performance Evaluation of the Conventional Method

In this section, we evaluate the conventional method under S/N = 23 dB. We define S/N as the ratio of the peak instantaneous signal power to the averaged noise power after

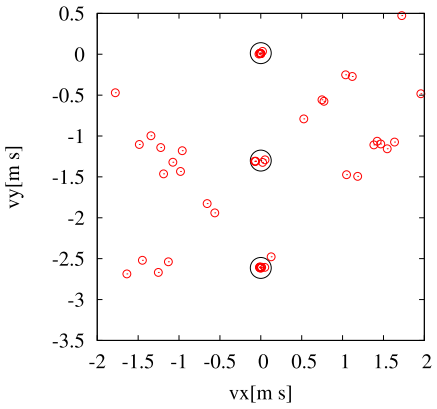

Fig. 5 Target velocities estimated from all possible combinations of radial velocities. The actual target velocities are shown as black circles.

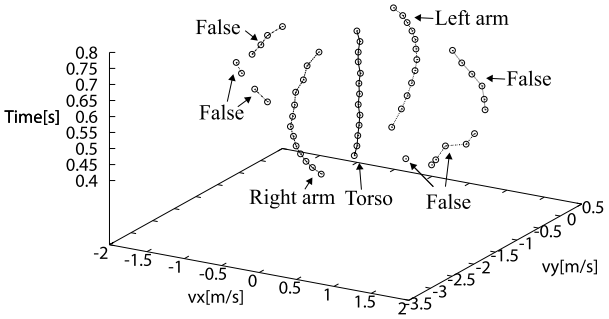

Fig. 6 Results of classification in the velocity space. v_x is the velocity of the x-axis, v_y is the velocity of the y-axis, and t is time.

applying the matched filter. Figure 4 is the spectrogram estimated by applying STFT to the signal received by interferometer 1. This figure shows the torso's constant radial velocity and the arms' sinusoidal radial velocity. We use the signal from $0.4 \leq t \leq 0.8$ for imaging, as the velocities are accurately separated in this period.

Figure 5 shows the distribution of velocity candidates at $t = 0.7$ s. The black circles denote the actual velocities, and the red circles represent the velocity candidates. This figure shows that many candidates are estimated around the actual velocities, whereas candidates are sparse in other places. However, this figure also shows that candidates are dense at some points, even though they are different from the actual velocities. Figure 6 shows the result of applying DBSCAN in the $v_x - v_y$ space at each time bin, applying DBSCAN to the median value of the extracted candidates in the $v_x - v_y - t$ space, and applying $\alpha - \beta$ tracking. The parameter values here are $D = 0.3$ m/s, $N_{\min} = 5$, $D_a = 0.6$ s, $D_b = 50\Delta t$, $N'_{\min} = 40$, $\alpha = 0.2$, and $\beta = 0.05$. The values of α and β are based on those in a Minimum-Variance filter [16]. This figure shows that those velocities that are equal to the actual velocities are connected to each other. However, some targets in Figs. 5 and 6 are only tracked for a short time, which means that these targets are likely to be false images. The false images are generated by erroneous target velocity estimates; multiple pairs of echoes coincidentally have consistent Doppler velocities, but this consistency only lasts for a short time. Nevertheless, some of the continuous velocity trajectories become too long to remove using DBSCAN in the $v_x - v_y - t$ space. This deteriorates the imaging quality as shown below.

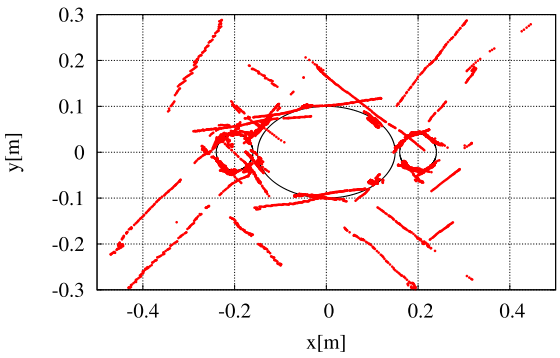

Fig. 7 Estimated image using the conventional method.

Figure 7 shows the estimated image using the classification results. From this figure, we can see that the shape of the target is expressed correctly, but some image estimates give a false shape because of misclassification. The conventional method suffers from false image estimation due to such misclassification of the scattering centers.

4. Proposed Method

The proposed method exploits the consistency of radial velocities to suppress false images resulting from the misclassification of scattering centers. The velocity of a scattering center $\boldsymbol{x}_{in}(t) = (x_{in}(t), y_{in}(t))$ is expressed as

$$v^{\mathrm{x}}_{\mathrm{x}in}(t) = \frac{\mathrm{d}}{\mathrm{d}t} x_{in}(t) \tag{13}$$

$$v^{\mathrm{x}}_{\mathrm{y}in}(t) = \frac{\mathrm{d}}{\mathrm{d}t} y_{in}(t), \tag{14}$$

where $v^{\mathrm{x}}_{\mathrm{x}in}(t)$ is the x-axis velocity of $\boldsymbol{x}_{in}(t)$, $v^{\mathrm{x}}_{\mathrm{x}in}(t)$ is the y-axis velocity of $\boldsymbol{x}_{in}(t)$, i denotes the index of interferometer estimating $\boldsymbol{x}_{in}(t)$, and n is the cluster number to which $\boldsymbol{x}_{in}(t)$ belongs. We can consider the scattering center's velocity to be the target velocity, as the rotation of the target and the scattering center's movement on the target can be neglected over short time periods. We have already estimated the target velocity using radial velocity combinations in the previous section.

We now explain how artifacts are generated by wrongly classified scattering centers. We can detect incorrect classifications by comparing two target velocity estimates obtained using the Doppler shift and the time-derivative of the target position, respectively. Figure 8 illustrates two different classifications of three scattering centers. The scattering centers are denoted as $\boldsymbol{x}_{ij}$ for the i-th interferometer and the j-th cluster. In this case, the scattering centers are estimated using interferometers 1, 2, and 3, respectively. If the scattering centers are classified correctly, $\boldsymbol{x}_1$ and $\boldsymbol{x}_2$ are included in the same cluster, encircled by a red solid line, whereas a

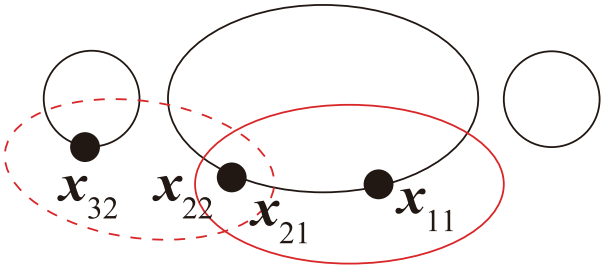

Fig. 8 An example of classified scattering centers.

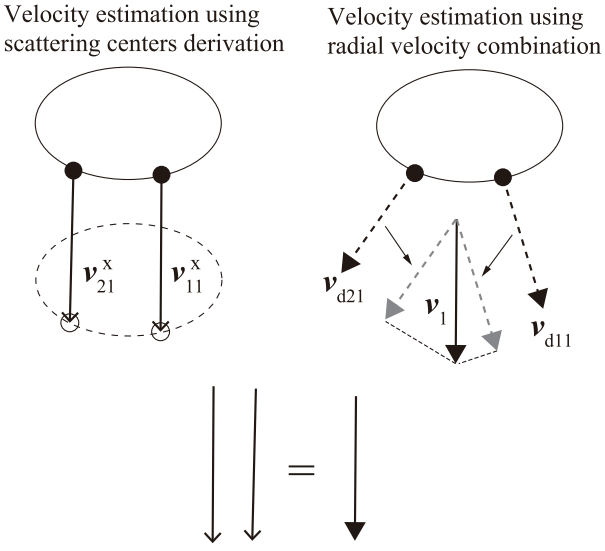

Fig. 9 Velocity comparison using the correct classification in Fig. 8.

wrong classification generates a cluster surrounded by a red dashed line.

Figures 9 and 10 are schematics of a comparison of the velocity estimates obtained using the Doppler shift and the time-derivative of the scattering center positions. In Fig. 9, $\boldsymbol{v}^{\mathrm{x}}_{11}$ and $\boldsymbol{v}^{\mathrm{x}}_{21}$ are estimated by differentiating the scattering center positions $\boldsymbol{x}_{11}$ and $\boldsymbol{x}_{21}$, whereas $\boldsymbol{v}_1$ is estimated using the Doppler shift of the echoes, which is independent of the position of the scattering center. This is because the positioning is achieved using the ranging function of a UWB radar, combined with the direction-of-arrival calculated from the phase difference. If targets 1 and 2 belong to the same cluster, estimates $\boldsymbol{v}^{\mathrm{x}}_{11}$, $\boldsymbol{v}^{\mathrm{x}}_{21}$, and $\boldsymbol{v}_1$ must be reasonably close to one another.

In contrast, Fig. 10 shows how we can detect wrongly classified scattering centers using the same approach. In this case, two scattering centers belong to different targets (an arm and torso). Here, the three target velocity estimates $\boldsymbol{v}^{\mathrm{x}}_{32}$, $\boldsymbol{v}^{\mathrm{x}}_{22}$, and $\boldsymbol{v}_2$ are different. In this way, we can effectively detect misclassifications by finding inconsistent combinations of velocities estimated from two different aspects of the received signal.

Next, we explain the details of our proposed method. We calculate $\boldsymbol{v}^{\mathrm{x}}_{in}(t)$ by subtracting the positions of the scattering centers. $\boldsymbol{v}^{\mathrm{x}}_{in}(t) = (v^{\mathrm{x}}_{\mathrm{x}in}(t), v^{\mathrm{x}}_{\mathrm{y}in}(t))$ is expressed as

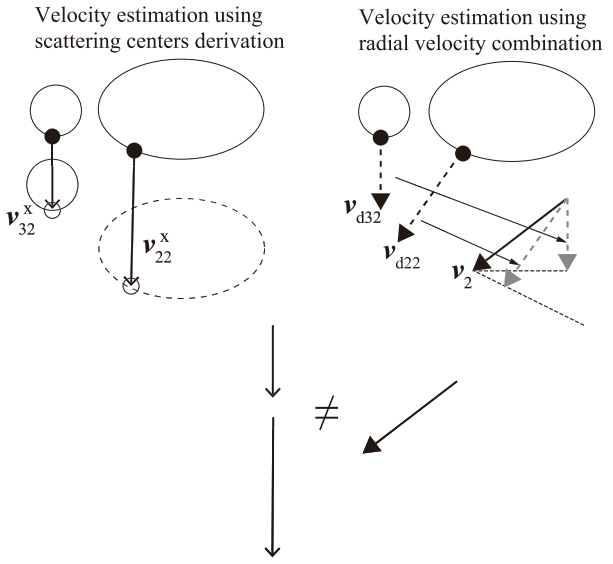

Fig. 10 Velocity comparison using the incorrect classification in Fig. 8.

$$v^{\mathrm{x}}_{\mathrm{x}in}(t) = \frac{x_{in}(t + \frac{t_{\mathrm{d}}}{2}) - x_{in}(t - \frac{t_{\mathrm{d}}}{2})}{t_{\mathrm{d}}} \tag{15}$$

$$v^{\mathrm{x}}_{\mathrm{y}in}(t) = \frac{y_{in}(t + \frac{t_{\mathrm{d}}}{2}) - y_{in}(t - \frac{t_{\mathrm{d}}}{2})}{t_{\mathrm{d}}}, \tag{16}$$

where t_{d} is the time period used for velocity estimation. This velocity estimates assume that the target rotation and the scattering center's movement on the target can be neglected for t_{d}. For stable velocity estimation, we set t_{d} to some large value. We then compare $\boldsymbol{v}^{\mathrm{x}}_{in}(t)$ with the value of $\boldsymbol{v}_{sn}(t)$, as estimated by the $\alpha - \beta$ filter described in the previous section, and extract $\boldsymbol{v}^{\mathrm{x}}_{in}(t)$ satisfying

$$|\boldsymbol{v}_{sn}(t) - \boldsymbol{v}^{\mathrm{x}}_{in}(t)| < d_{\mathrm{v}}, \tag{17}$$

where d_{v} is the velocity threshold. Finally, we consider $\boldsymbol{x}_{in}(t + \frac{t_{\mathrm{d}}}{2})$ and $\boldsymbol{x}_{in}(t - \frac{t_{\mathrm{d}}}{2})$ to be correctly classified, and remove the other classifications. Additionally, we remove misclassifications by removing clusters that do not include more than N_{v} scattering centers at t.

5. Performance Evaluation of the Proposed Method

Figure 11 shows the estimated torso velocity around $v_{\mathrm{x}} = 0$ m/s, $v_{\mathrm{y}} = -1.7$ m/s in Fig. 6 and the velocity estimated from the scattering centers associated with the torso velocity. We empirically set $t_{\mathrm{d}} = 50\Delta t$. Circles denote the torso's velocity as estimated from the radial velocities, and the other points express the velocity estimated from the scattering centers. This figure shows that the velocity estimated by the scattering centers is close to that estimated by radial velocities, because the scattering centers have been classified correctly.

In contrast, Fig. 12 shows the false velocity estimated around $v_{\mathrm{x}} = 1.3$ m/s, $v_{\mathrm{y}} = -1.0$ m/s in Fig. 6 and the velocity estimated from scattering centers associated with this false

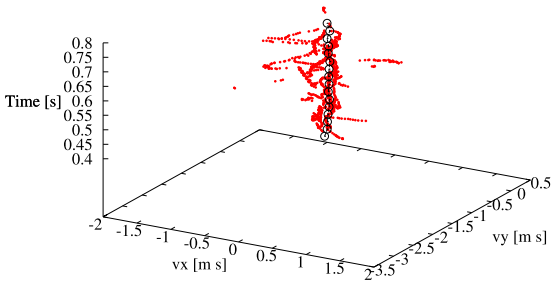

Fig. 11 Comparison between the torso velocities from radial velocities (black circles) and the velocities estimated from the differentiation of scattering center positions (other points).

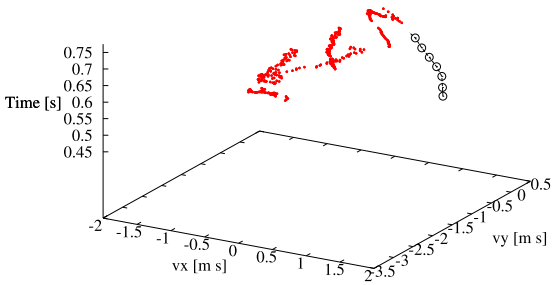

Fig. 12 Comparison between the false velocities from radial velocities (black circles) and the velocities estimated from the differentiation of scattering center positions (other points).

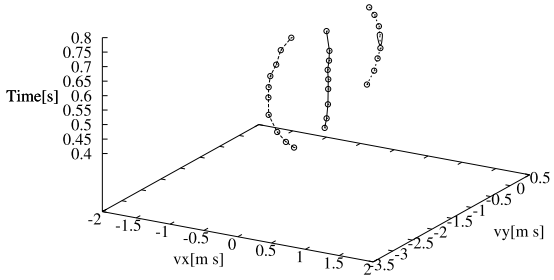

Fig. 13 Result of false velocity rejection using the proposed method, where $t_d = 50\Delta t$, $d_v = 0.3$ m/s, and $N_v = 3$.

velocity. This figure shows that the velocity estimated from the scattering centers is far from that estimated by the radial velocity. This discrepancy is caused by the incorrectly classified scattering centers. Figure 13 shows the velocities extracted by Eq. (17), where we empirically set $d_v = 0.3$ m/s and $N_v = 3$. We are able to extract the correct velocities and remove false velocities.

Figure 14 shows the image estimated from the classification results. The proposed method generates a clear image with a root mean square (RMS) error of 6.09 mm, whereas the image estimated by the conventional method has an RMS error of 100 mm. Next, we modify the value of S/N, and evaluate the noise tolerance of the proposed method. Figure 15 shows the RMS error for various values of S/N. We should note that there are no plots for $S/N < 10$ dB in Fig. 15. This is because the proposed method eliminates unreliable data by finding inconsistent velocity combinations.

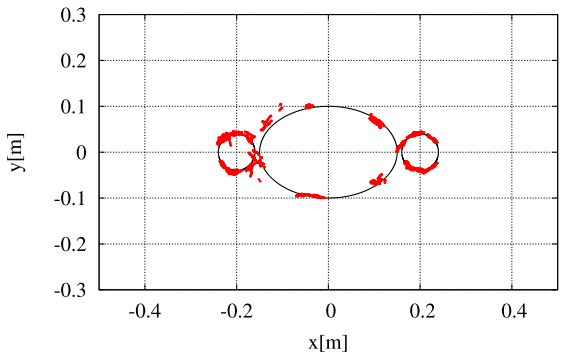

Fig. 14 Estimated image from the application of the proposed method to Fig. 7.

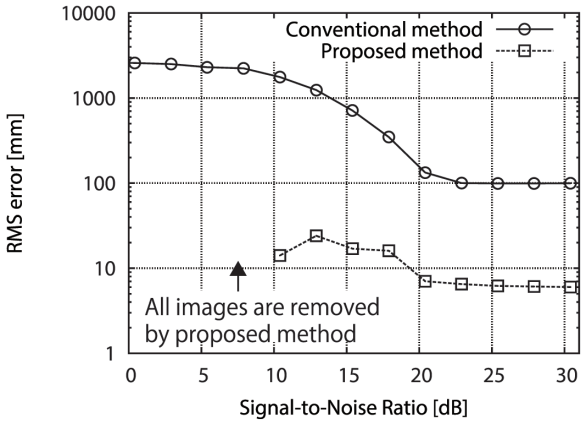

Fig. 15 Noise tolerance of the proposed method. Overall, the proposed method gives an improved image compared with the conventional method for this range of S/N.

Therefore, due to the low S/N, all of the image points have been rejected. This figure shows that the proposed method produces accurate images, compared with the conventional method, for all values of S/N. The images estimated using the proposed method have an RMS error less than 24.0 mm for $S/N \geq 10$ dB.

We can also evaluate the performance of the proposed method under other conditions. Figure 16 shows a scenario in which the human walks along trajectory 2 and trajectory 3. Trajectory 2 is the straight line at 30° from the y-axis, starting from (0.4 m, 2.7 m). Trajectory 3 is the straight line at 10° from the y-axis, starting from (0.74 m, 2.8 m). V_f, A_f, T_f, and θ_{f0} are the same as in Sect. 2. Figure 17 shows the image obtained for trajectory 2; with $S/N = 23$ dB, there is an RMS error of 6.79 mm. Figure 18 shows the image obtained for trajectory 3; with $S/N = 23$ dB, there is an RMS error of 7.37 mm. Figure 19 shows the RMS error for various values of S/N obtained for trajectories 2 and 3. The images estimated using the proposed method have an RMS error less than 21.8 mm for $S/N \geq 10$ dB. These results demonstrate the effectiveness of the proposed method under various conditions.

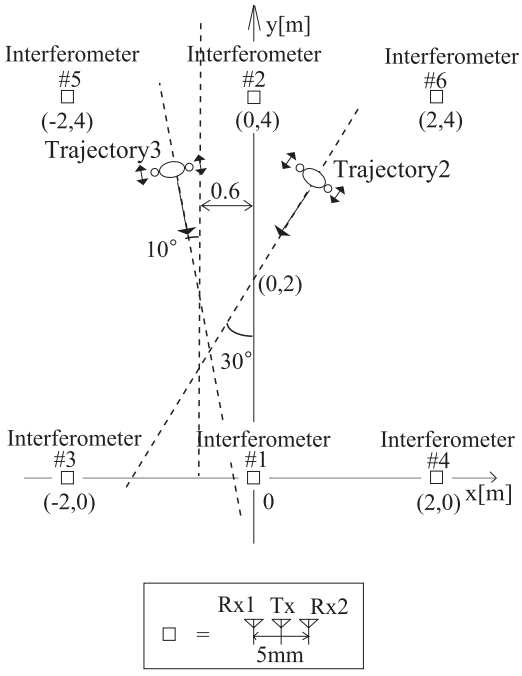

Fig. 16 System model for other walking trajectories.

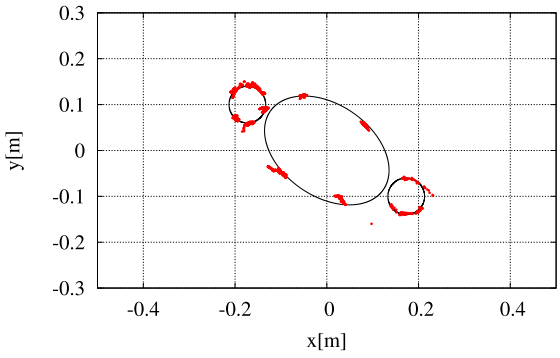

Fig. 17 Estimated image from the application of the proposed method under trajectory 2.

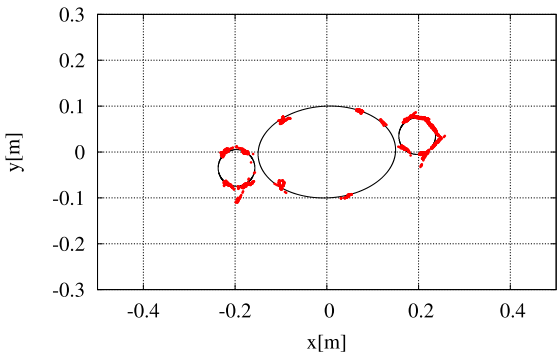

Fig. 18 Estimated image from the application of the proposed method under trajectory 3.

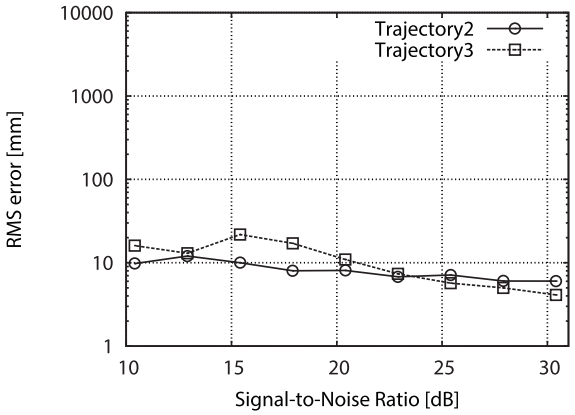

Fig. 19 Noise tolerance of the proposed method under another walking trajectory.

6. Discussion

In this study, the performance of the proposed method has been evaluated only with a simplified target model consisting of ellipses and circles. This is because the purpose of this study is to clarify the fundamental problems in imaging multiple targets in unknown motion, so that we can develop a robust and accurate imaging algorithm. Therefore, performing simulations using a more realistic human model is out of the scope of this study. In many existing studies on radar measurement of a human body, two models are mainly used: a model with point targets, and a model with cylinders. The former does not take into account the motion of scattering centers on the target surface, whereas the latter has only a few echoes, which simplifies the simulated signals. This study used the latter model with cylinders because the motion of scattering centers is essential in improving imaging performance as shown in [8]. An important part of our future research will be to analyze the effectiveness of our proposed approach even for a more realistic target model. Furthermore, although we assumed a 2-dimensional model only in this study, it would be important to extend the proposed approach to a 3-dimensional model. Sakamoto et al. proposed a 3-dimensional imaging using interferometry, taking advantage of moving scattering centers on the target surface [9]. This technique can be extended and integrated with the proposed method in this paper for developing a 3-dimensional imaging technology, which will be an important future task.

In our ray-tracing simulations, we considered only a single reflection without multipath echoes. This simplification can be justified by the following two reasons. First, the transmit antenna has a fan-shaped beam that has high and low directivities in the vertical and horizontal directions, respectively, which prevents multipath echoes from the floor and ceiling. Second, UWB radar signals have a wideband that corresponds to localized waveforms in the time domain, after applying a matched filter. This allows us to apply a time-gating and separate and suppress multipath echoes be-

cause they have time delay compared with direct echoes. In addition, the intensity of multipath echoes is smaller than that of direct echoes, which mitigates the effect of multipath interference. In contrast, there are some studies on even improving imaging performance by exploiting multipath echoes. For example, Kidera et al. [17] effectively employed multipath echoes to reconstruct images of targets in a shadow region, which cannot be seen directly from the antenna position. By combining this technique with the proposed method in this paper, it is expected that we can improve the imaging performance in a multipath-rich environment. The development of such a method is one of the important research topics in the future.

7. Conclusions

This paper has proposed a false image suppression method based on the consistency of the Doppler shift and the target's position. First, we showed that the conventional method produces false images if the wrong combination of target and scattering center is determined in the velocity space. The proposed method suppresses the false elements in the estimated image by exploiting contradictions between the actual target velocity and the radial velocity of the scattering centers in the false image. We evaluated the performance of the proposed method using a 2-dimensional simulation of a walking target consisting of a torso and two arms. The proposed method outputs clear images with an RMS error of 6.09 mm. These were clearly superior to the images given by the conventional method, which had an RMS error of 100 mm at $S/N = 23$ dB. Furthermore, we evaluated the noise tolerance of the proposed method, and revealed that the RMS error of the images produced by the proposed method was less than 24.0 mm for $S/N \geq 10$ dB. In future work, we will verify the proposed method using measurement data from an actual human body.

Acknowledgment

The authors would like to thank Dr. Kenshi Saho (Ritsumeikan University, Japan) for his help and advice with this work. This research was partially supported by the Supporting Program for Interaction-based Initiative Team Studies (SPIRITS) Japan-Netherlands joint development of sleep monitoring technology using ultra-wideband radar, the Center of Innovation Program (COI) The Last 5X Innovation R&D Center for a Smart, Happy, and Resilient Society, JSPS KAKENHI Grant Numbers 25249057 and 15K18077, and the R&D project for the expansion of radio spectrum resources for more efficient use of frequency resources for the future, supported by The Ministry of Internal Affairs and Communications, Japan.

References

[1] S. Nobuhara, Y. Tsuda, I. Ohama, and T. Matsuyama, "Multi-viewpoint silhouette extraction with 3D context-aware error detection, correction, and shadow suppression," IPSJ Trans. Comput. Vision and Appl., vol.1, pp.242–259, 2009.
[2] A. Mittal and L.S. Davis, "A general method for sensor planning in multi-sensor systems: Extension to random occlusion," Int. J. Comput. Vision., vol.76, no.1, pp.31–52, 2007.
[3] X. Zhuge and A.G. Yarovoy, "A sparse aperture MIMO-SAR-based UWB imaging system for concealed weapon detection," IEEE Trans. Geosci. Remote Sens., vol.49, no.1, pp.509–518, 2011.
[4] F. Gumbmann and L.-P. Schmidt, "Millimeter-wave imaging with optimized sparse periodic array for short-range applications," IEEE Trans. Geosci. Remote Sens., vol.49, no.10, pp.3629–3638, 2011.
[5] Y. Wang and A.E. Fathy, "Advanced system level simulation platform for three-dimensional UWB through-wall imaging SAR using time-domain approach," IEEE Trans. Geosci. Remote Sens., vol.50, no.5, pp.1986–2000, 2012.
[6] S. Bertl, A. Dallinger, and J. Detlefsen, "Broadband circular interferometric millimetre-wave ISAR for threat detection," Adv. Radio Sci., vol.5, pp.147–151, 2007.
[7] S. Bertl, A. Dallinger, and J. Detlefsen, "Interferometric focusing for the imaging of humans," IET Radar, Sonar & Navigation, vol.4, no.3, pp.457–463, 2010.
[8] T. Sakamoto, H. Yamazaki, and T. Sato, "Two-dimensional imaging of a pedestrian using multiple wideband Doppler interferometers with clustering-based echo association," IEICE Trans. Commun., vol.E98-B, no.9, pp.1795–1803, Sept. 2015.
[9] T. Sakamoto, Y. Matsuki, and T. Sato, "Method for the three-dimensional imaging of a moving target using an ultra-wideband radar with a small number of antennas," IEICE Trans. Commun., vol.E95-B, no.3, pp.972–979, March 2012.
[10] K. Saho, T. Sakamoto, T. Sato, K. Inoue, and T. Fukuda, "Pedestrian imaging using UWB Doppler radar interferometry," IEICE Trans. Commun., vol.E96-B, no.2, pp.613–623, Feb. 2013.
[11] V.C. Chen, D. Tahmoush, and W.J. Miceli, Radar Micro-Doppler Signature-Processing and Applications, The Institution of Engineering and Technology, 2014.
[12] M.G. Amin, Through-the-Wall Radar Imaging, CRC Press, 2011.
[13] P. van Dorp and F.C.A. Groen, "Human walking estimation with radar," IEE Proc., Radar Sonar Navig., vol.150, no.5, pp.356–365, 2003.
[14] R. Boulic, N.M. Thalmann, and D. Thalmann, "A global human walking model with real-time kinematic personification," The Visual Computer, vol.6, no.6, pp.344–358, 1990.
[15] M. Ester, H.-P. Kriegel, J. Sander, and X. Xu, "A densitybased algorithm for discovering clusters in large spatial databases with noise," Proc. 2nd International Conference on Knowledge Discovery and Data Mining, 1996.
[16] Y. Kosuge and M. Ito, "Evaluating an α–β filter in terms of increasing a track update-sampling rate and improving measurement accuracy," Electron. Comm. Jpn. Pt. I, vol.86, no.10, pp.10–20, 2003.
[17] S. Kidera, T. Sakamoto, and T. Sato, "Extended imaging algorithm based on aperture synthesis with double-scattered waves for UWB radars," IEEE Trans. Geosci. Remote Sens., vol.49, no.12, pp.5128–5139, 2011.

Appendix: Monostatic Interferometry Method

Figure A· 1 shows the principle of the monostatic interferometry method, which is used to estimate the scattering centers. The arrival distance between the antenna d is expressed as

$$d = d_{\mathrm{a}} \sin\theta, \tag{A· 1}$$

where d_{a} is the distance between the antenna and θ is the direction of arrival. d can be calculated by another equation,

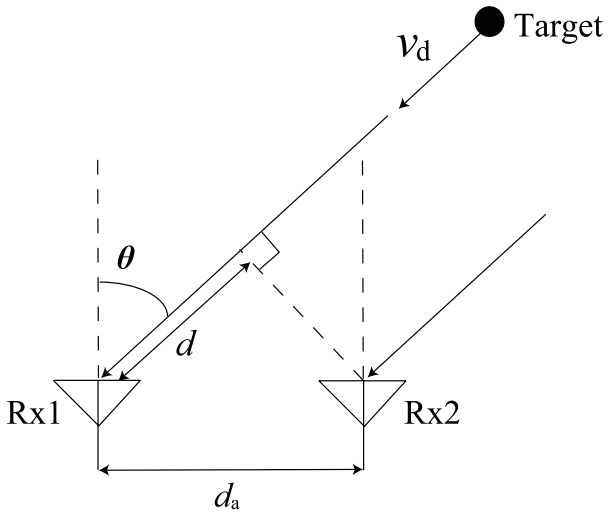

Fig. A· 1 Explanation of monostatic interferometry.

expressed as

$$d = \frac{c\Delta\phi}{2\pi f_0}, \tag{A· 2}$$

where $\Delta\phi$ is the phase difference between the antenna and f_0 is the center frequency. By connecting Eq. (A· 1) and Eq. (A· 2), θ can be calculated as

$$\theta = \sin^{-1}\left(\frac{c\Delta\phi}{2\pi d_a f_0}\right). \tag{A· 3}$$

Because our system assumes $d_a = 5\,\text{mm}$ and $\lambda = 11.4\,\text{mm}$, $d_a < \lambda/2$ holds, which means there are no grating lobes in this system.

Hiroki Yamazaki received his B.E. degree in 2013 from Kyoto University, Kyoto, Japan. He is currently working towards his M.S. degree at the Graduate School of Informatics, Kyoto University. His research interests include Doppler interferometry and ultrawideband radar imaging.

Takuya Sakamoto received the B.E. degree in electrical engineering from Kyoto University, Kyoto, Japan, in 2000 and the M.I. and Ph.D. degrees in communications and computer engineering from the Graduate School of Informatics, Kyoto University, in 2002 and 2005, respectively. Since 2015, he has been an Associate Professor at the Graduate School of Engineering, University of Hyogo, Himeji, Japan. From 2006 through 2015, he was an Assistant Professor at the Graduate School of Informatics, Kyoto University. From 2011 through 2013, he was also a Visiting Researcher at Delft University of Technology, Delft, The Netherlands. His current research interests lie in ultrawideband radar, radar imaging, and radar signal processing. Dr. Sakamoto is a member of the Institute of Electronics, Information and Communication Engineers of Japan (IEICE), the Institute of Electrical Engineers of Japan (IEEJ), and the Japan Society of Ultrasonics in Medicine. He received the Best Paper Award from the International Symposium on Antennas and Propagation (ISAP2004) in 2004, the Young Researcher's Award from the IEICE in 2007, the Best Presentation Award from the IEEJ in 2007, the Best Paper Award from the IEICE Communication Society in 2007, and the Best Paper Award from the International Symposium on Antennas and Propagation (ISAP2012) in 2012.

Hirofumi Taki received the M.D. degree and the Ph.D. degree in informatics from Kyoto University, Japan, in 2000 and 2007, respectively. He is currently a senior assistant professor of Graduate School of Biomedical Engineering at Tohoku University. His research interests include medical ultrasound, adaptive beamforming, and super-resolution imaging.

Toru Sato received his B.E., M.E., and Ph.D. degrees in electrical engineering from Kyoto University, Kyoto, Japan in 1976, 1978, and 1982, respectively. He has been with Kyoto University since 1983 and is currently a Professor in the Department of Communications and Computer Engineering, Graduate School of Informatics. His major research interests include system design and signal processing aspects of UWB radars, atmospheric radars, radar remote sensing of the atmosphere, and biomedical imaging. He is a fellow of the Institute of Electronics, Information, and Communication Engineers of Japan, and a member of the Society of Geomagnetism and Earth, Planetary and Space Sciences, the Japan Society for Aeronautical and Space Sciences, the Institute of Electrical and Electronics Engineers, and American Meteorological Society.